LBL-12548
UC-83

Lawrence Berkeley Laboratory
UNIVERSITY OF CALIFORNIA

Materials & Molecular
Research Division

NUCLEAR MATERIALS PROGRESS REPORTS FOR 1980

D.R. Olander

December 1980

Prepared for the U.S. Department of Energy under Contract W-7405-ENG-48

LBL-12548

NUCLEAR MATERIALS PROGRESS REPORTS

for 1980

Materials and Molecular Research
Division of the Lawrence Berkeley
Laboratory and the
Department of Nuclear Engineering
University of California-Berkeley
Berkeley, California 94720

D. R. Olander
Principal Investigator

This work was supported by the Director, Office of Energy Research, Office of Basic Energy Sciences, Materials Sciences Division of the U.S. Department of Energy under contract # W-7405-ENG-48

December 1980

CONTENTS

STRESS CORROSION CRACKING OF ZIRCALOY BY METAL IODIDES AND CADMIUM

Shih-Hsiung Shann

Even at low pressures, molecular iodine is an effective stress corrosion cracking (SCC) agent for zircaloy[1]. However, inside a reactor fuel pin, iodine is present mainly as cesium iodide. Also, metal iodides such as FeI_2 and AlI_3 could attain partial pressures in the mtorr range. Cadmium is a fission product which thermodynamics suggests should exist inside a fuel pin in the metallic state. Liquid cadmium is known to cause severe embrittlement of zircaloy. In an in-pile situation, however, the cladding is in contact with the vapor phase with low metal partial pressure rather than with a condensed phase. Therefore, a study of the stress rupture behavior of zircaloy in the presence of $AlI_3(g)$, $FeI_2(g)$, $CsI(g)$, and $Cd(g)$ was undertaken.

Tube specimens are internally pressurized with argon in order to produce a biaxial tensile stress state. Rupture lifetimes are measured as a function of stress, temperature, and partial pressure of the active chemical agent, which impinges as a molecular beam on a spot $\sim$1 cm diameter. The fracture mode is also observed by SEM.

Compared to control specimens at the same temperature and stress, failure times are greatly reduced by the presence of iron and aluminum iodides. For both iodine[1] and these iodides, there exists a stress (376 MPa), beyond which "burst-type" failure occurs. Lower stresses produce "pinhole-type" failures. However, fractography of both types of failures shows cleavage characteristics which are very different from the ductile-dimple fracture surface found in the absence of a corrosive agent. These three types of stress-rupture failures are shown in Fig. 1.

All specimens tested under cadmium exhibited burst-type failure and

the fracture surface showed brittle-type cleavage features. For cadmium, the rupture times were shorter than those of the control specimens but exhibited more scatter than those in iodine or the metal iodides. Fracture occured randomly inside the cadmium-affected region on the zircaloy specimen, unlike iodine and the iodides, where failure always took place at the center of molecular beam spot. There may be some unknown surface inhomogenity controlling the cadmium embrittlement process which is not present in SCC by iodine or metal iodides. Specimens cut from different tubes gave widely varying rupture times in cadmium, but tests using the same zircaloy tubes gave consistent results.

In cesium iodide tests, plots of time-to-failure versus stress did not show any decrease in comparison with control specimens. SEM fractography revealed completely ductile behavior, the same as that without a corrosive agent.

Greatly reduced failure times and brittle fractography are the two main features of stress corrosion cracking. On both counts, iodine, iron iodide, and aluminum iodide are stress corrosion cracking agents for zircaloy. However, cesium iodide is not. This behavior is consistent with the thermochemistry of the reactions[2]

$$0.55\ I_2(g) + Zr(s) \rightarrow ZrI_{1.1}(s) \qquad \Delta G^{o}_{600\ K} = -37.9 \text{ kcal/mole} \quad (1)$$

$$0.37\ A\ell I_3(g) + Zr(s) \rightarrow 0.37\ A\ell(s) + ZrI_{1.1}(s) \qquad \Delta G^{o}_{600\ K} = -11.0 \text{ kcal/mole} \quad (2)$$

$$0.55\ FeI_2(g) + Zr(s) \rightarrow 0.55\ Fe(s) + ZrI_{1.1}(s) \qquad \Delta G^{o}_{600\ K} = -32.7 \text{ kcal/mole} \quad (3)$$

$$1.1\ CsI(g) + Zr(s) \rightarrow 1.1\ Cs(\ell) + ZrI_{1.1}(s) \qquad \Delta G^{o}_{600\ K} = 29.4 \text{ kcal/mole} \quad (4)$$

The standard free energies suggest that the first three reactions are possible, but the last one is prohibited. This may be the reason why iodine, iron iodide and aluminium iodide, but not cesium iodide, can cause

SCC of zircaloy.

The rupture time data are correlated in terms of the crack growth model[3]:

$$\frac{da}{dt} = A\, p^n \exp(-E/RT) \exp(BK/T) \qquad (5)$$

Where a is the crack length, p is the partial pressure of the SCC agent, K is the stress intensity factor, and T is the temperature. A and B are constants. When integrated from initial length a_o to final length a_f at which the net section stress reaches the ultimate tensile stress, Eq. (5) gives the rupture time. The chemical or corrosion aspects of SCC is related to the reaction order n and activation energy E. These parameters are shown in Table 1.

The reaction orders for I_2 and FeI_2 are both unity, whereas that of AlI_3 is 2/3. These values reflect a rate-limiting surface chemical step with kinetics associated with the number of iodine atoms per molecule of SCC agent. Since it is unlikely that a nonlinear chemical reaction is involved in cadmium embrittlement (only alloying with the substrate metal is possible), the order for this species should be unity.

This crack growth model also predicts SCC experiments with variable loading and surface roughness[4].

Table 1. Chemical Parameters of Stress Corrosion Cracking of Zircaloy

SCC Agent	minimum partial pressure for SCC, torr	order, n	activation energy, E, Kcal/mole
I_2	1.4×10^{-3}	1.0 ± 0.1	7 ± 1
FeI_2	3.0×10^{-3}	0.9 ± 0.1	131 ± 5
AlI_3	1.4×10^{-3}	0.7 ± 0.1	-
Cd	7×10^{-3}	0.8 ± 0.1	54 ± 2

REFERENCES

1. S.-H. Shann and D. R. Olander, "Iodine Stress Corrosion Cracking of Zircaloy", Trans. Amer. Nucl. Soc. 32, 268 (1979).
2. D. Cubicciotti, R. L. Jones, and B. C. Syrett, "Chemical Aspects of Iodine-Induced Stress Corrosion Cracking of Zircaloy", ASTM Fifth Conference on "Zirconium in Industry", 1980.
3. A. G. Evans, and T. G. London, "Structure Ceramics", Progress in Material Science 21, 307 (1976).
4. S.-H. Shann, and D. R. Olander, "Correlation of Failure Times for Iodine SCC of Zircaloy", Nucl. Technol., to be published.

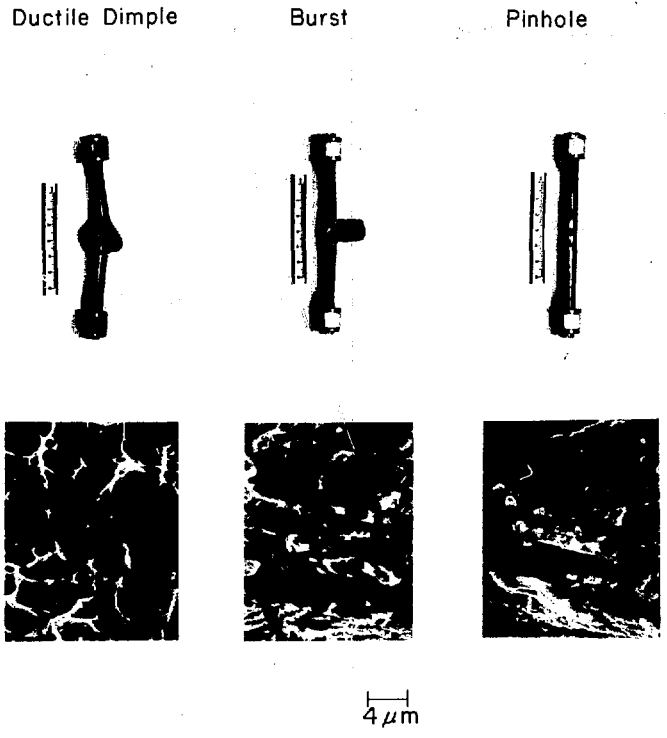

Fig. 1 Comparison of three types of fractures XBB800-14059A

POINT DEFECTS IN URANIUM DIOXIDE

K. C. Kim

The tracer diffusion coefficient of oxygen in UO_{2-x} has been measured using a diffusion couple consisting of two matched hypostoichiometric wafers, one enriched with oxygen-18 and the other normal, which were pressed together with a layer of liquid uranium. The uranium metal bond has a sufficiently high oxygen permeability so that it transports oxygen from one wafer to the other quite efficiently, thus eliminating an interface resistance in the diffusion couple.

In order not to perturb the stoichiometries of the wafers by the presence of liquid uranium, the experiments were performed only in the $U(\ell)+UO_{2-x}$ two-phase region. The stoichiometries were fixed automatically by the temperature and therefore the diffusion measurements apply only to oxide O/U ratios along the lower phase boundary

Following a diffusion anneal, the $^{18}O/(^{18}O + ^{16}O)$ profiles were determined by ion microprobe mass analysis. The data were fitted to the appropriate form of Fick's law for determination of the tracer diffusivity. Additional details of the experimental methods are given in Ref. 1.

In hypostoichiometric urania, oxygen self-diffusion occurs solely by the vacancy mechanism for which D is given by

$$D = D_o^V \theta_V (1 - \theta_V) \exp(-\Delta H_V/RT) \qquad (1)$$

where θ_V is vacancy concentration (x/2 in UO_{2-x}), ΔH_V is the activation energy of vacancy migration and D_o^V is a constant. Our diffusion measurements were well correlated by Eq. (1) (see Fig. 1), from which $D_o^V = 4.4 \times 10^{-4}$ cm^2/sec and $\Delta H_V = 11.7$ Kcal/mole were obtained. The activation energy

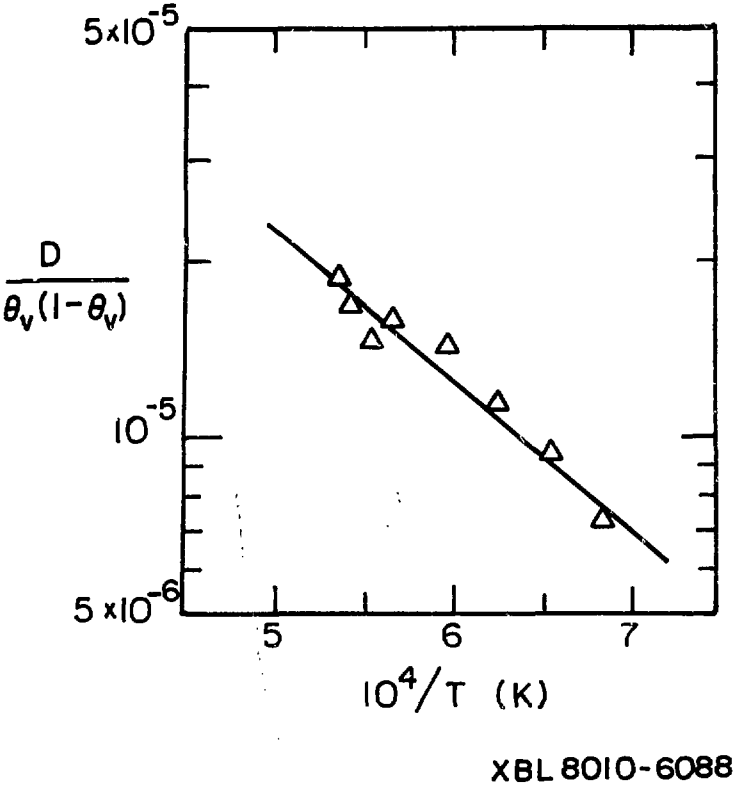

Fig. 1 Stoichiometry and temperature dependence of the oxygen tracer diffusivity in UO_{2-x}.

is in good agreement with those of other oxides of fluorite structure (CeO_{2-x} and PuO_{2-x}).

Assuming that oxygen diffusion in $UO_{2\pm x}$ proceeds simultaneously and independently by both vacancy and interstitial migration, the total oxygen diffusion coefficient can be expressed as the sum:

$$D = D_{(v)} + D_{(i)} \tag{2}$$

In substantially hypostoichiometric UO_{2-x}, $D_{(i)} \simeq 0$ and the diffusivity is that given by Eq. (1). Similarly, in highly hyperstoichiometric UO_{2+x}, $D_{(v)} \simeq 0$ and the observed oxygen diffusivity reduces to:

$$D \simeq D_{(i)} = D_o^i \theta_i(1-\theta_i) \exp(-\Delta H_i/RT) \tag{3}$$

where θ_i is the interstitial concentration. Values of

$D_o^i = 4.7 \times 10^{-3}$ cm^2/s and $\Delta H_i = 21.8$ Kcal/mole were obtained by re-analyzing the existing oxygen diffusion data on UO_{2+x} [2,3]. From the above equations, the oxygen diffusivity for all O/U ratios is given by:

$$D = 4.4 \times 10^{-4} \theta_v(1-\theta_v) \exp(-11700/RT) + 4.7 \times 10^{-3} \theta_i(1-\theta_i) \exp(-21800/RT) \tag{4}$$

In oxides far removed from stoichiometry, the point defect concentrations θ_v and θ_i are simply related to the nonstoichiometry parameter x in $UO_{2\pm x}$. However, in stoichiometric UO_2, the point defect concentration is determined by the thermodynamics of anion Frenkel disorder. The law of mass action for this defect reaction is

$$K_F = \frac{\theta_v}{1-\theta_v} \cdot \frac{\theta_i}{1-\theta_i} = \exp(\Delta S_F/R) \exp(-\Delta H_F/RT) \tag{5}$$

which, with the condition of electroneutrality, $\theta_i = 2\theta_v$, determines θ_i and θ_v. Thus D can be expressed in terms of the Frenkel entropy and enthalpy (ΔS_F and ΔH_F) by using Eq. (5) in Eq. (4). Oxygen diffusion data for stoichiometric UO_2 [4] were fitted in this manner to obtain $\Delta S_F = 18.2 \pm 7.3$ e.u. and $\Delta H_F = 85.0 \pm 9.2$ Kcal/mole. Using these values of ΔS_F and ΔH_F, contributions of vacancies ($D_{(v)}$) and interstitials ($D_{(i)}$) to the oxygen diffusion coefficient in stoichiometric UO_2 were calculated. At very low temperatures, vacancies are the primary species that contribute to oxygen mobility. In the temperature range 800-1800°C, neither of the species is completely predominant and at 1400°C the contributions of the two species are approximately equal.

It is well known that the enthalpy of UO_2 displays an unusually rapid increase from 1500°K to 3100°K, which cannot be explained by lattice vibrations. Szwarc [5] attributed all of this excess enthalpy to Frenkel disorder, from which he deduced the Frenkel entropy and energy of $\Delta S_F = 14.8 \pm 0.8$ e.u. and $\Delta H_F = 71.3 \pm 2.2$ Kcal/mole, respectively. Recently, however, a series of attempts have been made to re-interpret the excess enthalpy of UO_2 in terms of electronic excitation [6-8] Although quantitative results could not be obtained because the electronic structure of UO_2 is not well established, it was demonstrated that the electronic contribution to the enthalpy could be significant, in which case the component of the Frenkel disorder is less than determined by Szwarc [5]. Our values of the Frenkel energy and entropy are in line with this theory because they yield lower population of Frenkel defects than predicted by Szwarc's model [5] and therefore their contribution to the enthalpy is also smaller. After removing the lattice contribution from the measured excess enthalpies and applying the 2-band model of the

electronic contribution (6), a band gap of 2.0 ev and an effective mass of 7.6 m_e were obtained. The former figure is in good agreement with the values obtained from electrical conductivity data (9).

References:

1. K. Kim and D.R. Olander, MMRD Annual Report, LBL-10000, p.222 (1979)
2. P. Contamin, J.J. Backmann, and J.F. Marin, J. Nucl. Mater., 42 (1972) 54
3. G.E. Murch, D.H. Bradhurst, and H.J. deBruin, Phil. Mag., 32 (1975) 1141
4. J.F. Marin and P. Contamin, J. Nucl. Mater., 30 (1969) 16
5. R. Szwarc, J. Phys. Chem. Solids, 30 (1969) 705
6. D.A. MacInnes, J. Nucl. Mater., 78(1978) 225
7. R.J. Thorn, G.H. Winslow and J.S. Ziomek, J. Nucl. Mater., 87 (1979) 416
8. D.A. MacInnes and C.R.A. Catlow, J. Nucl. Mater., 89 (1980) 354
9. J.I. Bates, C.A. Hinman, and T. Kawada, J. Am. Ceram. Soc. 50 (1967) 652

THE SURFACE CHEMISTRY OF EPITAXIAL SILICON DEPOSITION BY THERMAL CRACKING OF SILANE

by M. Farnaam

I. Introduction

Thermal cracking of silicon-containing gases such as silane at pressures in the torr range occurs via reactions such as:

$$SiH_4(g) \longrightarrow Si + 2H_2(g)$$

Processes based on these reactions have provided satisfactory means for epitaxial growth of silicon for production of integrated circuits and solar energy devices. However, the need for production of higher quality solar cells[1], and better control in fabrication of very large scale integrated circuits (VLSI) will most probably guide the epitaxial deposition process towards higher vacuum levels and molecular beam techniques.

Obviously, conventional methods of investigation of the thermal cracking reactions[2,3,4] can no longer be useful in analyzing the molecular beam deposition techniques, hence revealing the need for modulated molecular beam experiments[5].

II. Experimental

A. Residence Time Measurement

In order to deduce the residence time of SiH_4 molecules on the surface, a series of experiments utilizing a mixed beam of SiH_4/Ar was performed at room temperature and high temperatures. In these experiments the relative phase lag of SiH_2^+ (as an indication of SiH_4) with respect to Ar^+ was measured. The data were corrected for the transit phase lags due to the travel times of the molecules from chopper to target, target to mass spectrometer, and

through the mass spectrometer. The first two corrections were made using a computer program based on the theoretical calculation of Harrison, Hummer and Fite[6], and also the assumption that at high temperatures the thermal accommodation coefficients are equal to 1. The phase lag in the mass spectrometer was determined by the method of Ref. 7.

The results were reproducible and are shown in Figs. 1 and 2. Assuming that the Ar atoms reflect off the crystal instantaneously, these data appear to suggest a negative residence time for the SiH_4 molecules on the surface.

In order to clarify this unacceptable conclusion, similar experiments were performed using a mixture of Ar/Ne. The results are shown in Figs. 3 and 4, which this time suggest a negative residence time for Ne atoms. Apparently there are some effects which are not being accounted for properly.

B. Isotope Exchange Experiments

In order to investigate whether hydrogen atoms are produced on the surface during the thermal cracking of silane, a mixed beam of SiH_4/SiD_4 was used which at high temperature ($\sim$1400 K) resulted in detection of HD^+ signal by mass spectrometer. A comparable HD^+ signal was detected at room temperature indicating the presence of molecules such as SiD_3H, SiD_2H_2.... etc. in the SiD_4 container (which has 98 atom % Deuterium).

This problem could easily be solved by using a combination of modulated SiH_4 beam and steady SiD_4 beam, but since the nozzle tube carrying steady SiD_4 beam contaminates on the target at high temperatures, this method was ruled out, therefore requiring other techniques.

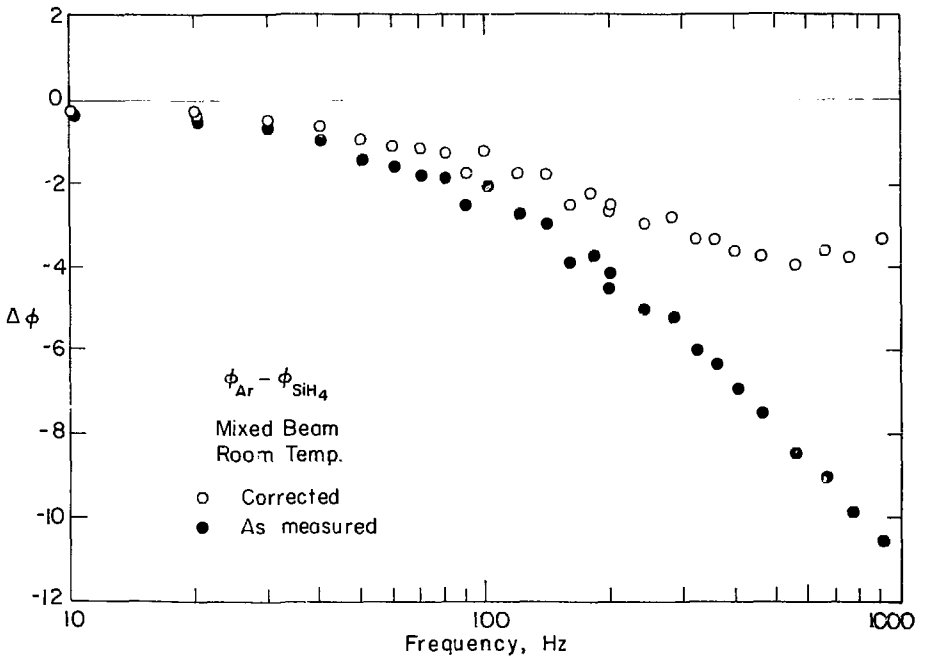

XBL 812-5281

Fig. 1 Argon phase lag with respect to silane vs. frequency in a mixed beam room temperature experiment

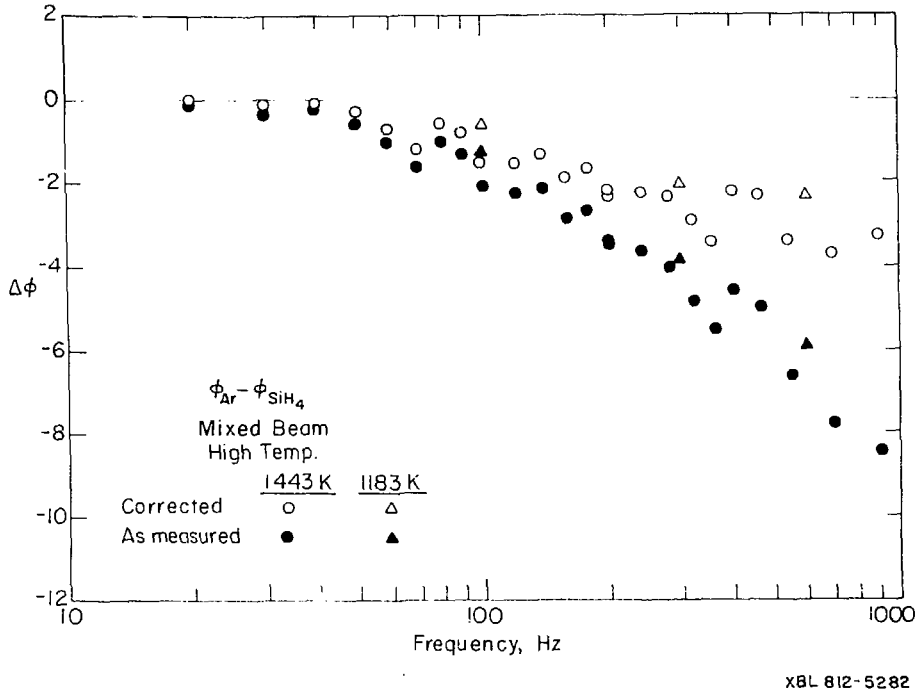

Fig. 2 Argon phase lag with respect to silane vs. frequency in a mixed beam room temperature experiment

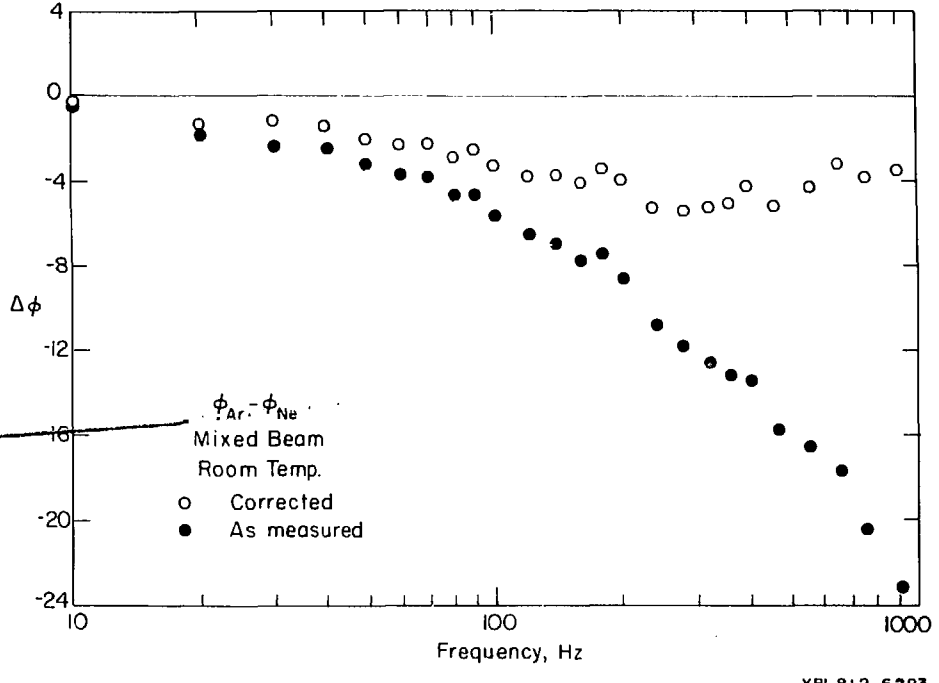

Fig. 3 Argon phase lag with respect to neon vs. frequency in a mixed beam room temperature experiment

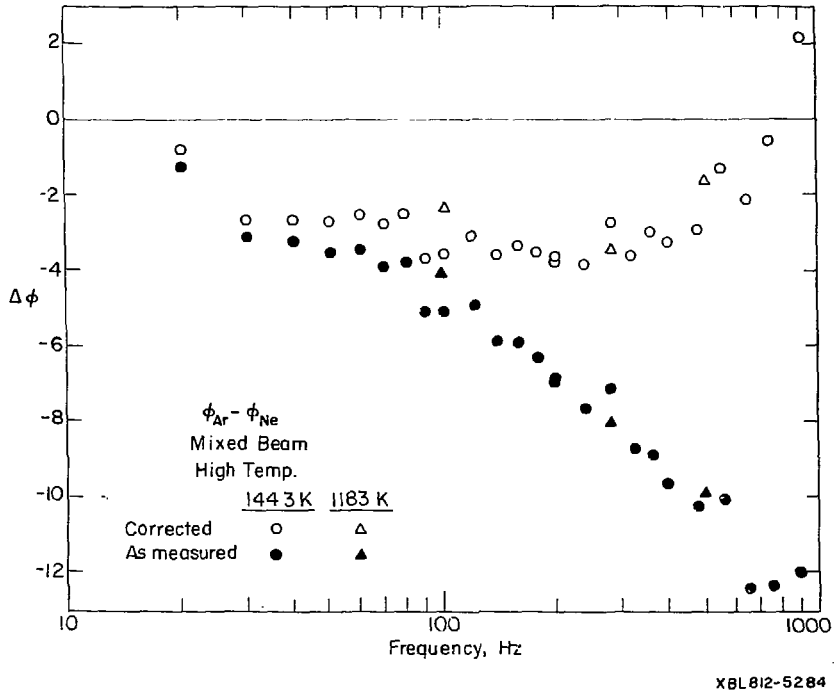

Fig. 4 Argon phase lag with respect to neon vs. frequency in a mixed beam high temperature experiment

C. Surface Steps

At the end of a 1400 K experiment, the electron beam heater was inadvertantly turned down at a much faster rate than usual, causing the crystal temperature to drop at the rate of about 80 k/s. Subsequent observation of the crystal under optical microscope revealed one major and two minor groups of parallel lines along $\langle 1\bar{1}0 \rangle$ directions. The spacings of the lines in the major group were about 5 μm for shallow lines and about 70 μm for deeper lines. The Scanning Electron Microscope revealed that these lines were in fact steps on the surface.

III. Planned Experiments:

The following experiments may be useful in answering some of the questions raised by previous experiments.

1. The residence time experiments will be continued with a mixture of Ar/He at two drastically different ratios of Ar to He pressures. This would help determine whether the gas pressure ratio in the mixture is an important factor due to effects such as the seeded beam phenomenon. Also, performing Ne/He mixture experiments would provide information required to establish an empirical relation for calculation of transit phase lags of the inert gases. This empirical relation would then be applied to the values in Figs. 1 and 2 as an additional correction factor which would finally result in a more reliable calculation of the silane residence time.
2. The problem of HD^+ signal measurements encountered in the SiH_4/SiD_4 experiment might be solved by calculating the fraction of SiH_nD_{4-n} molecules[8], using the measured cracking pattern of SiD_4 (2 atom % H) beam. It would then be possible to calculate the

portion of the HD^+ signal actually produced due to the production of hydrogen atoms during a SiH_4/SiD_4 mixed beam experiment at high temperatures.

3. More experiments are required to determine whether the steps observed on the surface at the end of the high temperature experiment were in fact the actual steps on the surface present during the two dimensional evaporation process which were then frozen in place due to the fast rate of cooling the crystal. If this is the case, measurement of their spacing could be helpful in the calculation of some of the thermodynamical properties of the (111) face of the silicon crystal[9].

REFERENCES

1) H. Ehrenreich & J. Martin, Physics Today, Sept. 1979, p. 25.

2) B. A. Joyce, et al, Phil. Mag. 14, 289, 301 (1966) & 15, 1167 (1967).

3) R. C. Henderson, et al, Surf. Sci. 30, 310 (1972).

4) R. F. C. Farrow, J. Electrochem, Soc. 121, 899 (1974).

5) R. H. Jones, D. R. Olander, W. J. Siekhaus & J. A. Schwarz, J. Vac. Sci. Technol., 9, 1429 (1972).

6) Harrison, Hummer and Fite, J. Chem. Phys. 41, 2567, (1964).

7) R. H. Jones, Ph.D. Thesis, LBL-104 (1971).

8) Stelio Villani, "Isotope Separation", published by ANS (1976).

9) Hirth & Pound, J. Chem. Phys. 26, 1216 (1957).

THE KINETICS OF LASER PULSE VAPORIZATION OF UO_2

C. H. Tsai

I. INTRODUCTION

Laser pulse heating technique has been playing an increasingly important role in simulating transient, kinetic processes, especially in high temperature thermodynamics studies. The mass spectrometry technique is being developed in this lab to investigate the vaporization kinetics of uranium oxide (1). The preliminary results of Knudsen cell steady state heating at low temperatures have been used, based upon the assumption of thermodynamic equilibrium, to obtain ionization cross sections and fragmentation patterns. The results are compared with the direct measurements by Blackburn(2) and Pattoret(3), and a set of ionization cross section ratios and fragmentation ratios are recommended for use in the evaluation of high temperature mass spectrometer measurements.

Temperature measurement by fast-response optical pyrometry has been found in a fairly good agreement with the numerical solution of the coupled heat conduction and oxygen diffusion problems(1,4). The computer code has been modified for better generality, and is briefly described here. The code has been applied to laser pulse heating of UO_2 as well as the first wall design of the Inertial Confinement Fusion concept. The results of the sample calculations are presented and discussed.

II. MASS SPECTROMETER CALIBRATION

An EAI QUAD 250 quadrupole mass spectrometer with Bendix electron multiplier has been used for the anlysis of the laser-evaporated vapor(1,6). For UO_2 vaporization, the mass numbers are tuned for

286 (UO_3), 270 (UO_2), 254 (UO), 238 (U) and perhaps 32 (O_2). A Knudsen cell consisting of an electrically heated tungsten tube filled with UO_2 powder was used for the calibration in the temperature range 1800°C to 2400°C(6). Fig. 1 shows the results. It is the intention of this report to fit the calibration measurement to the well-established low temperature thermodynamic information based on the assumption of thermodynamic equilibrium to obtain the fragmentation patterns of the three gaseous uranium oxide molecules.

The vapor in equilibrium with UO_2(S) is composed of six species, namely, UO_3, UO_2, UO, U, O and O_2. Of these, UO_3, UO_2 and UO are the most abundant. Upon impact by high energy electrons in the ionizer, UO_3 neutral molecules may crack and be ionized into lower mass ions, such as UO_2^+, UO^+, U^+; UO_2 molecules may crack and be ionized into UO^+, U^+; and UO to U^+. The ions produced from the same mass of neutral species (e.g. UO_3^+ from UO_3) are called "parent ions", while those produced from higher mass neutrals (e.g. UO_2^+ from UO_3) are called "fragment ions". The measured current of some mass is the sum of the parent ions and fragment ions from higher mass.

The ratios of the signals can be expressed as: (3 = UO_3, 2 = UO_2, 1 = UO and 0 = U)

$$\frac{S_3}{S_2} = \frac{(\frac{P_3}{P_2})C_3F_{33}}{C_2F_{22}+(\frac{P_3}{P_2})C_3F_{33}} \qquad (1)$$

$$\frac{S_1}{S_2} = \frac{(\frac{P_1}{P_2})C_1F_{11}+C_2F_{21}+(\frac{P_3}{P_2})C_3F_{31}}{C_2F_{22}+(\frac{P_3}{P_2})C_3F_{32}} \qquad (2)$$

$$\frac{S_0}{S_2} = \frac{(\frac{P_0}{P_2})C_0F_{00} + (\frac{P_1}{P_2})C_1F_{10} + C_2F_{20} + (\frac{P_3}{P_2})C_3F_{30}}{C_2F_{22} + (\frac{P_3}{P_2})C_3F_{32}} \qquad (3)$$

where S_i = measured current signal of i^+ ion

P_i = partial pressure of i neutral molecule in the Knudsen cell

C_i = relative total ionization cross section of i neutral to that of UO_2 ($= \sigma_i/\sigma_2$)

F_{ii} = fraction of i^+ ions from ionization of i neutral

F_{ki} = fraction of i^+ ions from ionization of k neutral ($m_k > m_i$)

i = 3, 2, 1, 0

The current ratios S_3/S_2, S_1/S_2, S_0/S_2 for different temperatures can be obtained from the curves in Fig. 1. The pressure ratios P_3/P_2, P_1/P_2, P_0/P_2 can be obtained from the thermophysical calculations for the congruently vaporizing compositions for different temperatures. The C's are from Pattoret(3):

$$(\sigma\gamma)_0/(\sigma\gamma)_1/(\sigma\gamma)_2/(\sigma\gamma)_3 = 1.15 : 0.80 : 0.55 : 0.38 \qquad (4)$$

where σ_i = total ionization cross section of i neutral

γ_i = relative electron multiplier gain for i^+ ion

i.e.

$$C_3 = 0.69,\ C_2 = 1,\ C_1 = 1.45,\ C_0 = 2.09 \qquad (5)$$

Therefore, an optimal set of F_{ij}'s can be obtained by fitting eqs. (1)-(3) to the data on Fig. 1:

$F_{33} = 0.13$

$F_{32} = 0.6$

$F_{31} = 0.2$

$F_{30} = 0.07$

$F_{22} = 0.6$

$F_{21} = 0.21$

$F_{20} = 0.19$

$F_{11} = 0.88$

$F_{10} = 0.12$

From the slopes of the curves in Fig. 1, we obtain the heat of sublimation of 139.6 kcal/mol for UO_3, 128.7 kcal/mol for UO_2, 100 kcal/mol for UO and 109.9 kcal/mol for U; the literature gives 140 kcal/mol for UO_2.

Table 1 shows the comparison of this work with the fragmentation fractions measured by Blackburn(2) and Pattoret(3).

TABLE 1: The Fragmentation Fractions of U-C System

	Blackburn	Pattoret	This work
F_{33}	0.1042	0.2	0.13
F_{32}	0.4385	0.6	0.6
F_{31}	0.4583	0.16	0.2
F_{30}	0	0.04	0.07
F_{22}	0.5	0.625	0.6
F_{21}	0.5	0.281	0.21
F_{20}	0	0.094	0.19
F_{11}	0.667	0.88	0.88
F_{10}	0.333	0.12	0.12

The result of this work agrees quite well with Patoret(3). To show the effect of the fragmentation in the vapor pressure measurement by mass spectrometry based on the above calibration, the ratios of the partial pressure of i species considering fragmentation to the values without fragmentation are:

UO_3 ----- 7.7

UO_2 ----- 1.7

UO ----- 0.74

U ----- 0.28

III. NUMERICAL SIMULATION OF TRANSIENT LASER VAPORIZATION

Laser radiation is considered a surface heat source. In most of the cases the power density is so high that the surface layer melts and the enormous temperature gradient makes the assumption of constant thermal properties inadequate. Surface boundary recession and thermal radiation heat loss become so important that the boundary value problem becomes highly non-linear. Therefore, the analytic solution (5,6) is no longer a good approximation. Besides, in a multi-component system, the strong vaporization is usually highly incongruent and creates a composition gradient in the bulk of the compound and, if the composition is an important factor on the thermodynamic behaviour of the vaporizing material, the mass diffusion process has to be considered coupled with the heat conduction process. The numerical computation is the only way to solve this problem of highly non-linearity and complexity. The system consists of one-dimensional heat conduction and oxygen diffusion in a semi-infinite slab occupying the region $x \geq 0$, where the moving boundary x=0 is irradiated by a pulse of laser beam propagating in the x-direction. As described in detail in Ref. 4, the

system consists of the coupled boundary value problems of heat and mass transport. Thermal diffusion (Soret and Dufour) effects of oxygen are negligible.

Figs. 2-5 show the results of the "STAR" (Surface Temperature And composition Ratio calculation) computer run in which the incident laser total energy is 30 Joules with the pulse shape shown in Fig. 6, and the effective laser spot area is 0.5 cm^2. Figs. 2 and 4 also show the results of the "SURFT" (SURFace Temperature calculation) computer run which assumed no composition change so that only heat conduction equation is solved and the laser has the same characteristics as the run in "STAR".

The difference of the maximum surface temperature from "STAR" and "SURFT" is about 200K, which is mainly due to the vaporization effect in the ablation terms and to the fact that the rate of vaporization is a function not only of temperature but also of the composition.

Fig. 7 shows the maximum surface temperature as a function of the total incident laser energy calculated from both "STAR" and "SURFT". At the low energy (or low temperature) range where vaporization effect is relatively unimportant, the two calculations give consistent results, while at high energy, the discrepancy of as much as 200 - 300 K is attributed to the ablation effect.

The computer program has been designed to deal with (i) thermal conduction problem only ("SURFT"), or a diffusion process at constant temperature only ("SURFR"), or both ("STAR"), (ii) the same kind of problems with different materials and (iii) different kind of problems (e.g. different differential equations, boundary conditions, or/and different type of heat sources - laser or ion beam, surface or volumetric source) with different materials. For instance, the possible

applications might be the thermal analysis of the first wall in a CTR, the thermal analysis of laser-driven micro-explosions, the thermal analysis of electron beam heating, the thermal and mass transport analysis of laser annealing or electron beam annealing in semiconductor ion implantation and other applications of pulse heating techniques in material processing.

Thermal analysis of a first wall design (7-9) was completed and compared with the current design based on approximate analytic solutions. Details are given in Ref. 4.

REFERENCES

1. C. H. Tsai and D. R. Olander, LBL-8580, UC-13, 1978; LBL-11030, UC-25, 1979.
2. G. E. Blackburn and P. M. Danielson, J. Chem. Phys. 56 (1972) 6156.
3. A. Pattoret, Ph. D. Thesis, Universite Libre de Bruxelles, 1969, pp. 30-36.
4. C. H. Tsai, "Numerical Simulation of Transient, Incongruent Vaporization Induced by High Power Laser", LBL-12125, UC-21, (1981)
5. H. S. Carslaw and J. C. Jaeger, "Conduction of Heat in Solid", Oxford University Press, London and N.Y. 1959.
6. Ramon P. DePaula, M. S. Thesis, U. C. Berkeley, 1979.
7. G. R. Hopkins, Trans. ANS 22, 163 (1975).
8. G. R. Hopkins, R. J. Price, R. E. Bullock and J. A. Dalessandro, Proc. third topical meeting on the technology of the controlled Nuclear Fusion, Vol. 1, CONF-780508 (1978) pp. 324-333.
9. R. W. Conn, et al, UWFDM-229, U. of Wisc. 1977.

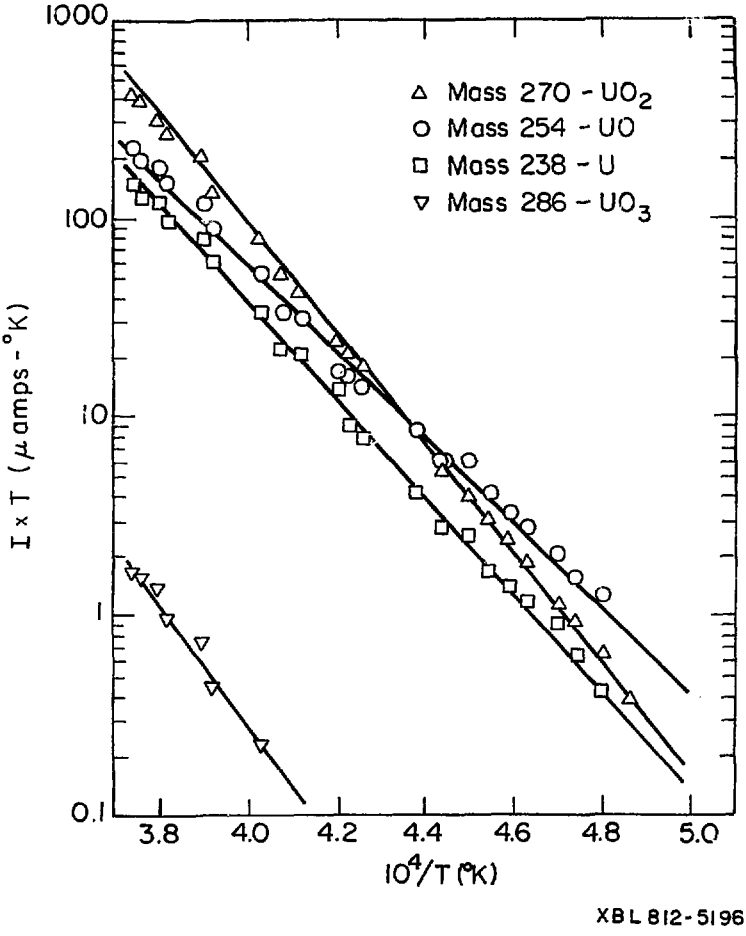

Fig. 1 Mass spectrometer calibration curve for UO_3, UO_2, UO and U.

SURFACE TEMPERATURE OF LASER PULSING ON UO2 Fig. 2

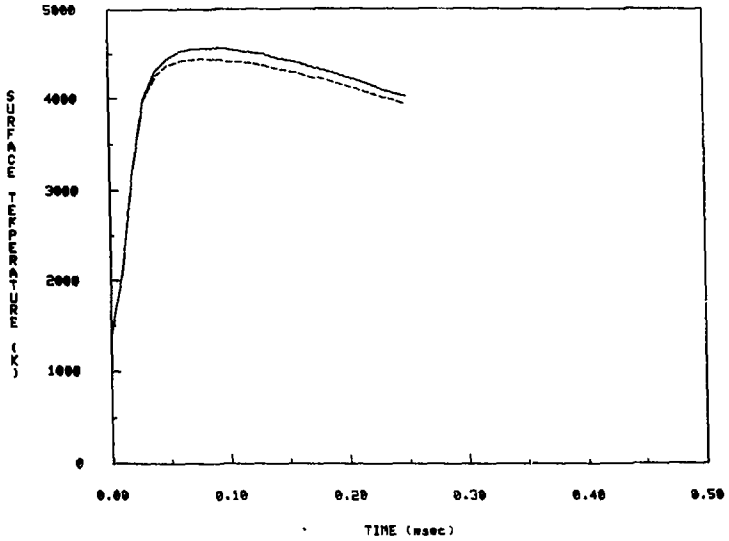

NUMERICAL SOLUTIONS
E = 30 Joules

——— FROM STAR
------ FROM SURFT

The Surface Temperature of UO_2 with Time for Real Laser Pulse with Ablation, Radiation Heat Loss and Variable Properties.

SURFACE COMPOSITION OF LASER PULSING ON UO2 Fig. 3

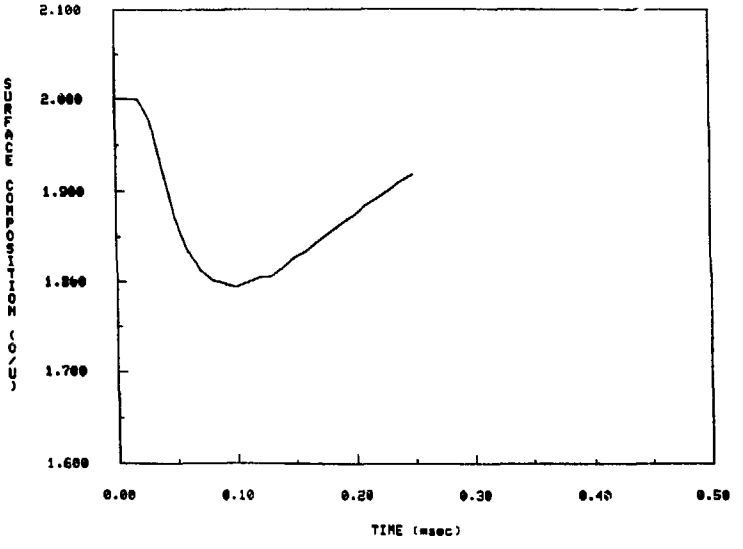

CALCULATED FROM STAR
E = 30 Joules

The Surface Composition of UO_2 with Time for Real Laser Pulse with Incongruent Vaporization

TEMPERATURE PROFILE OF LASER PULSING ON UO2 Fig. 4

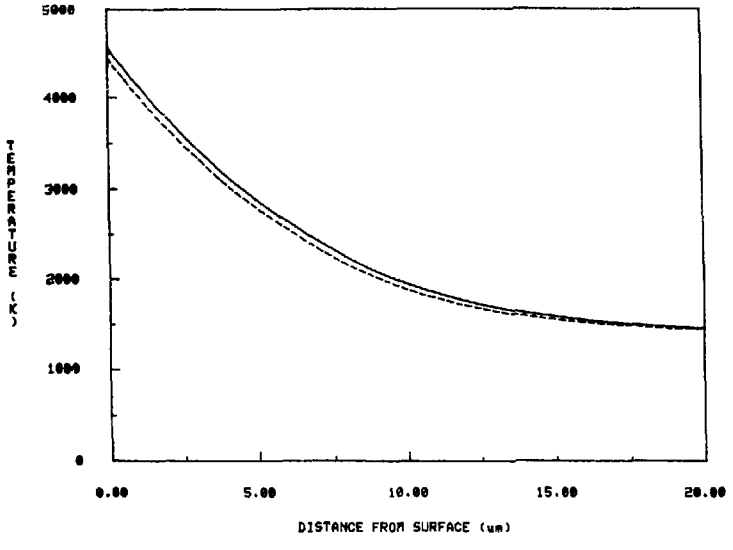

The Temperature Profile of UO_2 Subject to Total Energy 30 Joule Laser Surface Heating

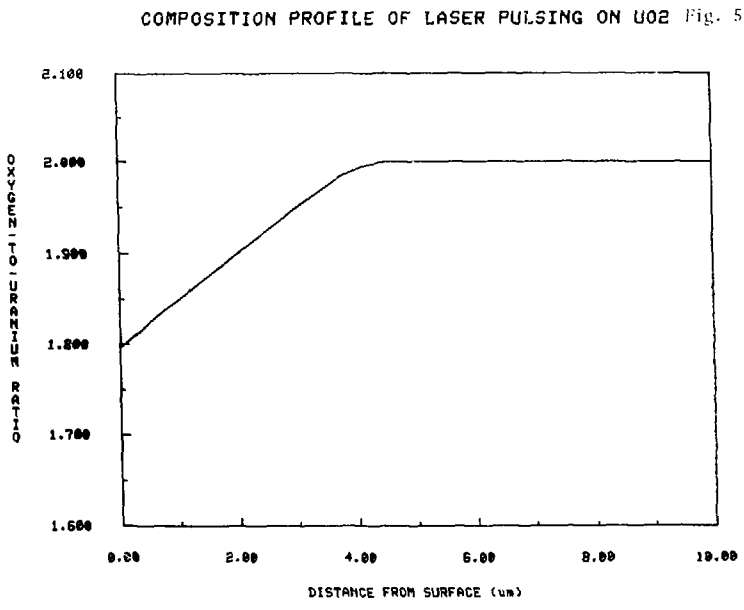

The Oxygen-to-Uranium Ratio Profile of UO_2 Subject to Total Energy 30 Joule Laser Surface Heating with Incongruent Vaporization

LASER PULSE SHAPE FROM POWER TRACE Fig. 6

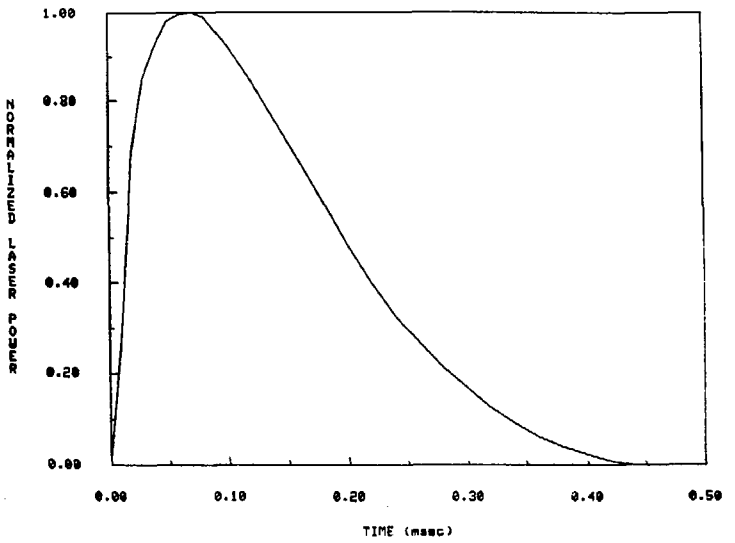

The Normalized Laser Pulse Shape with Time

MAX SURFACE TEMPERATURE OF LASER PULSING ON UO2 Fig. 7

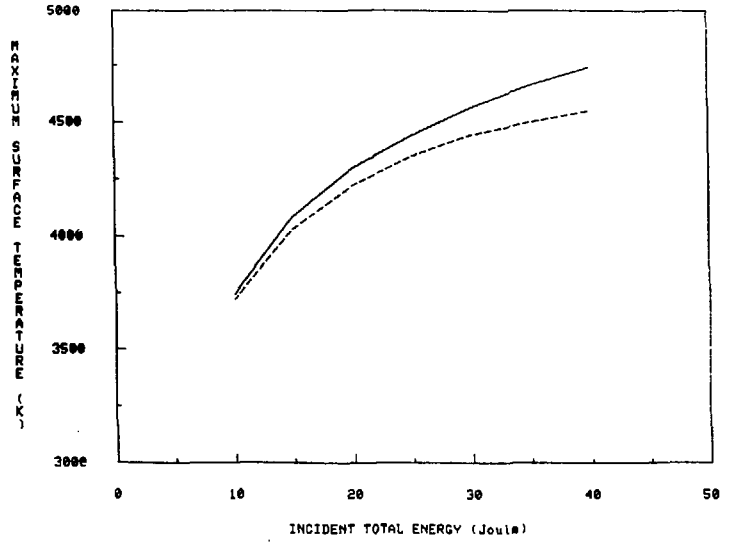

The Maximum Surface Temperature of UO_2 vs Incident Total Energy

STUDY OF THE KINETICS OF UC VAPORIZATION AT TEMPERATURES ABOVE MELTING POINT USING LASER HEATING TECHNIQUE

F. Tehranian

INTRODUCTION

As part of the reactor safety analysis, the vapor pressure of uranium carbides up to 5000°K is needed in order to predict the behavior of the fuel in a Hypothetical Core Disruptive Accident (HCDA) and estimate the energy release during the power transient of a prompt critical excursion.

While there is extensive data on properties of uranium carbon system below the melting temperature (2780 K), the only high temperature experimental work has been done by OHSE et. al. [1], who measured the total vapor pressure of $UC_{1.08}$ up to 7000 K by the laser pulse-heating technique. Fig. (1) shows their result along with the low temperature extrapolation by Finn et. al. [2].

The laser technique which is being used here is equipped with a quadropole mass spectrometer by which we are able to obtain information on the individual vapor species in the plume.

Experimental Method: The experimental apparatus consists of three main parts a) The laser and equipment for energy and power measurement, b) vacuum chambers containing the target and mass spectrometer and c) the signal recording equipment.

The laser is a Nd-glass laser with wavelength of 1.06 μ and pulse duration of about 1 m sec. It is aligned and focused on a UC target in the vacuum chamber at pressure 10^{-7} torr at an angle of 45° to the beam. The target is heated by an electron beam heater up to 1800°C for several

hours before the laser is shot in order to prevent cracking due to thermal stresses and also to decontaminate the sample of oxygen. The vapor species emitted are detected by the mass spectrometer which is located in the detection chamber. The temperature of the target is measured by a fast optical pyrometer.

UC Samples: The uranium carbide samples are 0.7 cm in diameter and ~1.4 mm thick and have a density of 90% of the theoretical volume. The samples are kept in an argon atmosphere in a glove box. The polishing of the samples is also done under inert atmosphere using Hyprez oil as the lubricant to prevent oxygen and moisture contamination.

Laser Pulse Characteristics: Each laser pulse is characterized by a) pulse shape, b) pulse energy and c) power density profile. This information is used as input to a computer program for calculating the temperature profile in the sample, and needs to be known in each set of experiments.

The energy and power of the laser pulse are measured by a photodiode which is calibrated by a calorimeter. Since the pulse shape changes by changing the high voltage fitters are used to change the laser pulse energy in order to achieve the same normalized pulse shape, shown in Fig. (2). By integrating the pulse shape we are able to find the maximum power for each pulse energy (P_{max})

To measure the radial profile of the energy density [I(r)] on the target, we used the razor blade technique described in previous annual reports. Fig. (3) shows the result of this measurement. This profile is used to find an effective area (A_{eff}) defined as

$$A_{eff} = \int_0^R \frac{I(r)}{I(0)} 2\pi r dr$$

A value of 5.11 mm^2 is obtained for the effective area.

A_{eff}, P_{max} and the normalized pulse shape obtained are used in the computer program.

References:

1. Ohse, R. W., Babelot, J. F., Long, K. A., Magill J., Vapor Pressure Measurement of Uranium Carbides up to 7000 K using laser pulse heating. European Institute for Tranuranium Elements, Postfach 2266, D-75000 Karlsruhe, Federal Republic of Germany.
2. Finn, P. A., Sheth, A., Winslow, G., and Liebowitz, L., Advanced LMFBR Fuels, P. 189, Topical Meeting Proceedings, Tucson, Arizona, Oct. 10-13, 1977. Edited by Leary, J., and Kittle, H.

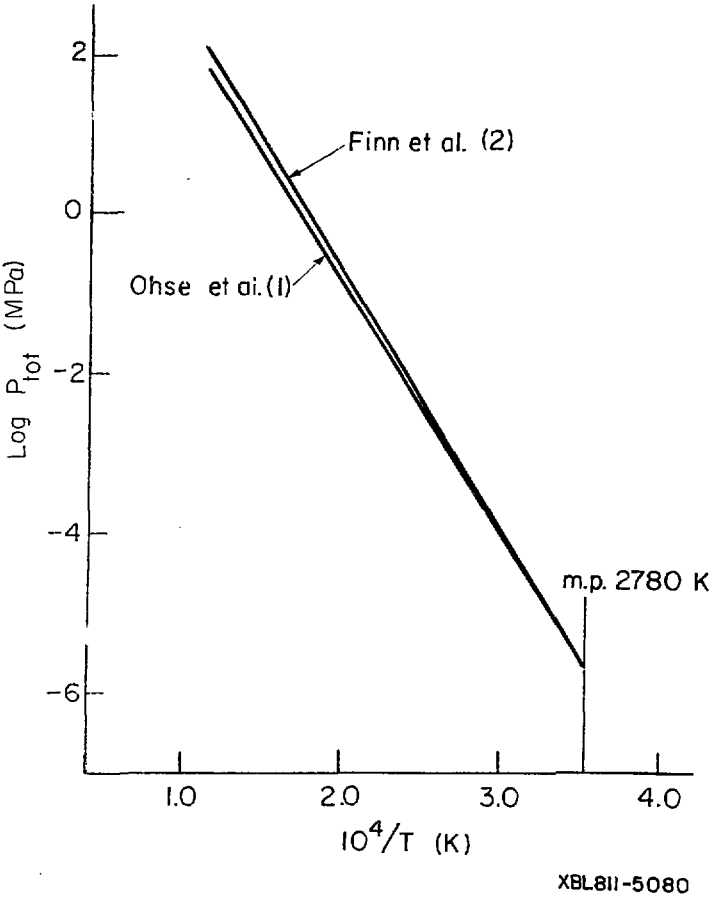

Fig. 1. Total vapor pressure over UC

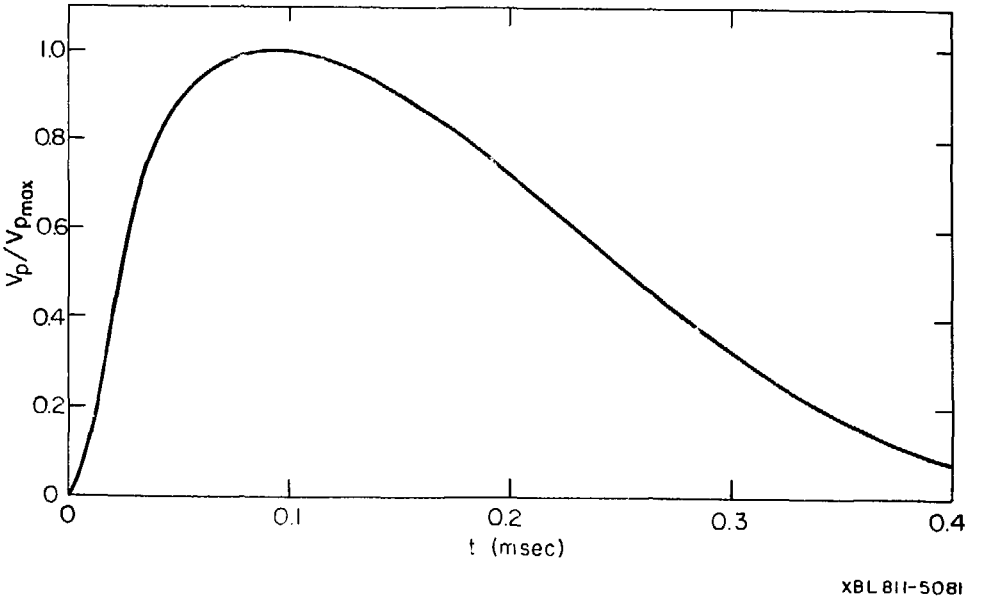

Fig. 2 Laser pulse shape.

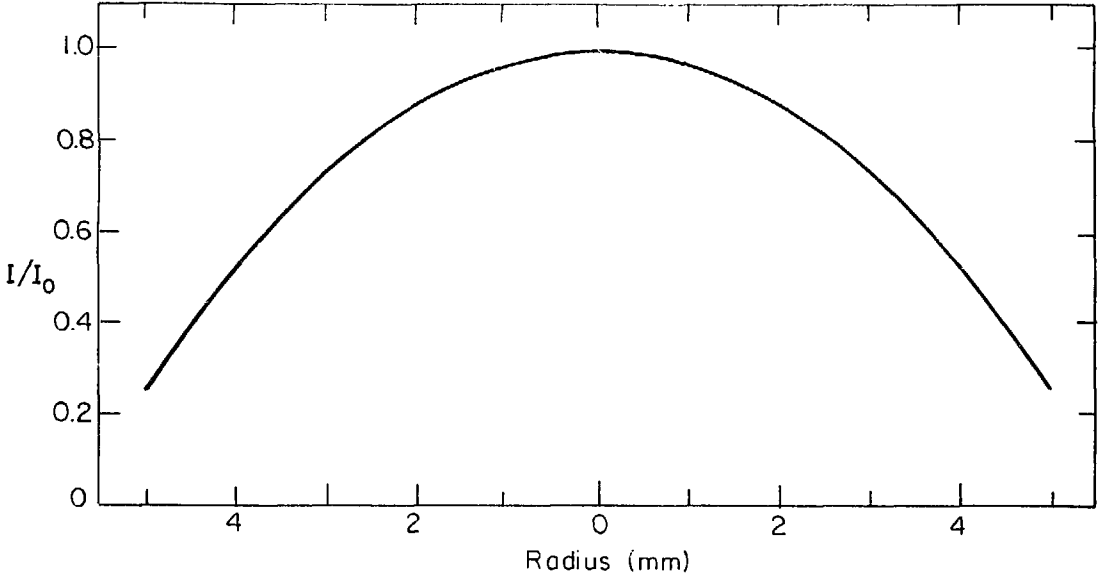

Fig. 3 Radial profile at the target
$\frac{I}{I_0} = 1 - 0.03\ r^2$

XBL 811-5082

RELEASE OF WATER VAPOR FROM URANIUM DIOXIDE

Douglas Sherman

Uranium dioxide is known to adsorb water vapor rapidly from the air. When the UO_2 is subsequently heated the water is released. This water is a potential source of hydrogen which can cause hydriding of zircaloy cladding. Another source of water in UO_2 fuel pellets is the gaseous atmosphere used during sintering. In order to control the stoichiometry during sintering, either cracked ammonia or wet hydrogen is used, so hydrogen-bearing gases may be retained by the solid during densification at high temperature ($\sim$1750°C).

Uranium dioxide samples of differing porosities and microstructures were exposed to D_2O instead of H_2O in order to avoid measurement difficulties due to the large H_2O background in the vacuum system. In order to simulate the retention of water during sintering, other UO_2 samples were fabricated in a D_2/D_2O atmosphere. The characteristics of the specimens are shown in Table 1. The type-A and B pellets were used to simulate physical adsorption of water vapor, and type-C pellets studied hydrogen/water vapor retention during sintering. The type-D pellets served as blanks. The sintering conditions of the type-A pellets resulted in high open and closed porosities and a measurable BET surface area. The type B and D pellets were prepared under standard commercial fuel sintering conditions and resulted in low closed and essentially no open porosity. Their surface area was less than the limit of detection of the BET method. The type-A and B pellets were immersed in liquid D_2O after being outgassed in vacuum in order to physically adsorb water on their surfaces. The

type-C and D pellets were not treated after sintering.

Details of the apparatus are given in Ref. 1. Briefly, the pellets prepared as described above are heated in a tungsten crucible which is suspended in a vacuum furnace. The outgased D_2O effuses from the exit capillary of the furnace and is chopped to produce a modulated molecular beam which is detected by a mass spectrometer in the vacuum. The mass spectrometer is calibrated with a known flow rate of neon.

The experimental results showed a large release of physically adsorbed water for the high porosity type-A pellets and a negligible release for the low porosity type-B pellets.

The results for the outgassing of the type-C pellets during a series of anneals at successively higher temperatures is shown in Fig. 1. The 5 anneals (at 910°C to 1860°C) show abrupt release rate increases upon changing temperature followed by a roughly exponential decay.

The model used to describe the release process is desorption-limited. The water contained in the UO_2 is assumed to be located on multiple binding sites with a distribution of binding energies. Each site has a characteristic desorption rate constant, B, which is related to the binding energy E and pre-exponential factor A by:

$$B = Ae^{-E/kT}$$

The sites which bind water in UO_2 are characterized by the distributions of the parameters A and E. In order to simplify the analysis, the site distribution is assumed to have a constant pre-exponential factor A and the binding energies are distributed according to the function:

$n_s(E)dE$ = number of binding sites/g UO_2 with binding energies between E and E+dE

In order to analyze the constant-temperature anneals, this distribution is converted to a distribution of desorption rate constants, which is defined by:

$N_s(B)$ = number of sites/g UO_2 with desorption constants between B and B+dB at temperature T.

The distribution of desorption rate constants, $N_s(B)$, is determined from the binding energy distribution $n_s(E)$ and the anneal temperature.

In the analysis, a binding energy distribution is assumed. For each constant temperature anneal, this $n_s(E)$ guess gives a corresponding rate constant distribution $N_s(B)$ which in turn yields a release rate prediction. The objective of this analysis is to deduce the distribution $n_s(E)$ which gives the best fit to the release rate data for the 5 annealing steps of Fig. 1. Fig. 2 shows the binding site distribution that produced the best fit to the release data. The dashed curves in Fig. 1 show the computer fit to the data. The release rate data suggest that water retained by UO_2 during the sintering process contains a major component bound with $\sim$ 25 kcal/mole, and smaller components with binding energies of $\sim$ 40 and $\sim$ 53 kcal/mole.

References:

1. A. Srivastava and D.R. Olander, Trans. Amer. Nucl. Soc. 28, 216 (1978)

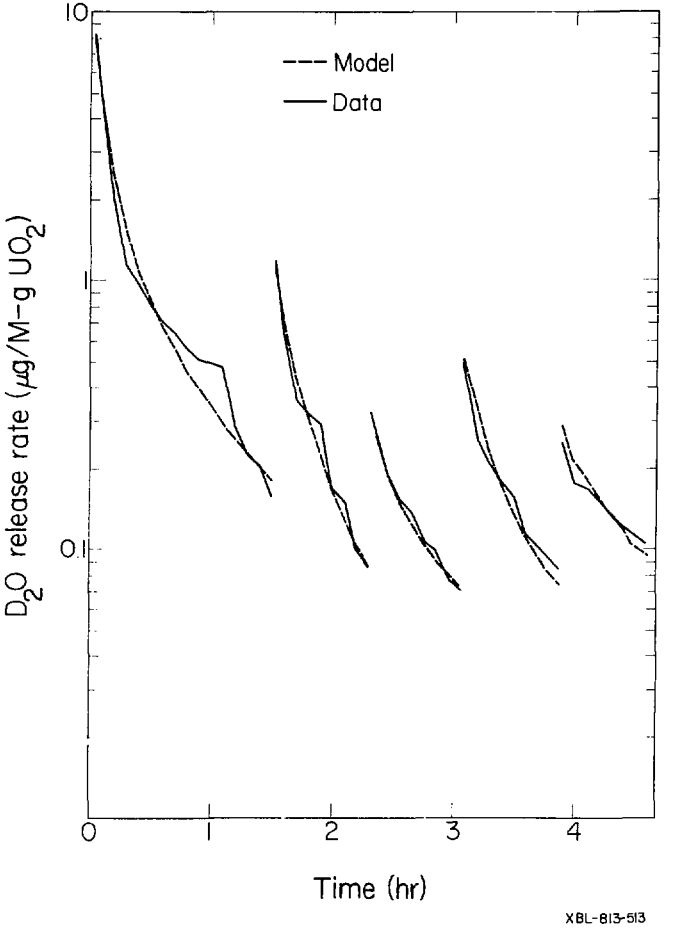

Fig. 1 Kinetics of release of D_2O from UO_2 for 5 sequential constant temperature anneals

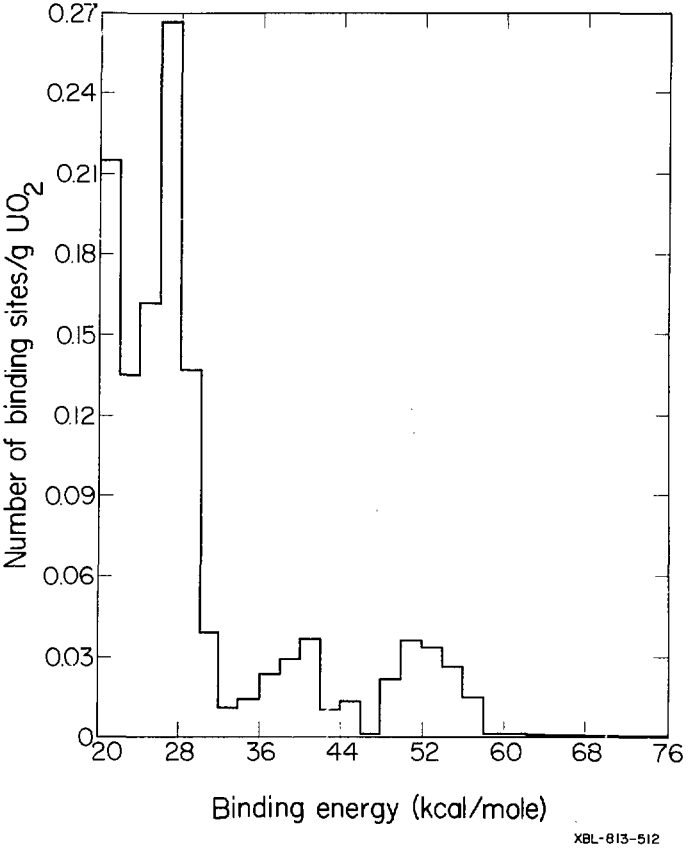

Fig. 2 Distribution of water binding sites in UO_2

Table 1. UO_2 Specimens used in Outgassing Experiments

Type	Sintering Conditions	Porosity, % Open	Porosity, % Closed	BET surface area, m^2/g	D_2O loading method
A	1450°C, in H_2O/H_2, 2 hrs	5.1	15	0.14	immersion in boiling D_2O liquid
B	1750°C, in H_2O/H_2, 6 hrs	<0.1	7	< 0.01	immersion in boiling D_2O liquid
C	1750°C, in D_2O/D_2, 6 hrs	<0.1	7	< 0.01	D_2 sintering gas saturated with D_2O at 30 - 40°C
D	1750°C, in H_2O/H_2, 6 hrs	<0.1	7	< 0.01	none

THE REDISTRIBUTION OF RUTHENIUM IN UO_2 IN A TEMPERATURE GRADIENT

S. Y. Zhou

1. INTRODUCTION

It is well known that at high temperature and in a high temperature gradient the fission products in oxide fuel elements redistribute. The redistribution of these species has a significant influence on the performance of the fuel element. It is believed that thermal diffusion might play an important role in the redistribution of fission products dissolved in the fuel matrix. By using estimated parameters, Nichols, et al[1] theoretically analyzed the kinetics of redistribution of barium in irradiated UO_2 fuel based on thermal diffusion. Beisswenger, et al[2] studied the thermodiffusion in system UO_2-CeO_2.

Ruthenium is one of the fission products and together with an Rh,Tc,Pd and Mo, forms metallic inclusions distributed along grain boundaries or in the central void of the fuel element. Originally these fission products are uniformly produced throughout the element; why they move to the high temperature region and by what mechanism are not known. It was believed that the metallic inclusions migrate bodily in UO_2 at high temperatures and in steep temperature gradients[3-5]. However, a recent experiment has shown that metallic inclusions such as W,Mo,Ru do not migrate as entities. The present study is concerned with the temperature gradient-driven mobility of ruthenium in UO_2 as a means of better understanding the redistribution of metallic fission products in oxide fuel elements.

2. EXPERIMENTAL

The experiments were carried out in the high temperature - temperature gradient furnace described in Ref. 6. By heating the top of the

tungsten crucible and cooling the bottom end of the sample with a molybdenum rod, the furnace can produce 1500 - 2000^{O} K/CM temperature gradient.

The samples were made by General Electric Company. Before sintering, nuclear grade UO_2 powders were mixed uniformly with 99% pure Ru powders having particle sizes ranging between 1μm - 10μm. The samples were sintered in hydrogen atmosphere at 1700^{O}C for 4 hours. Two 0.001" thick rhenium foil disks were placed on the top and the bottom of the sample in order to prevent possible reaction between tungsten crucible and UO_2.

Each experiment lasted about 28 to 34 hours in order to produce detectable redistribution. After the experiments, the samples were either cut with a diamond saw into slices 200μm - 300μm thick or else layers of about the same thickness were ground off one by one for X-ray fluorescence analysis, which had previously been calibrated with standard Ru/UO_2 samples. Optical microscopy and SEM were used for visual examination of the samples before and after the experiments.

3. RESULTS

A. Temperature Gradient Experiments

Three experiments were conducted at different temperatures, temperature gradients, sample thicknesses, and times. Initially the concentration of Ru in the samples was uniform. After the experiments, the Ru particles partially dissolved into the UO_2 grain boundaries, and Ru redistributed along the thermal gradient. Microscopic observation of the sample showed that the radii of the Ru particles did not change; instead, voids were created in the centers of the particles. One of the Ru concentration profiles is shown in Fig. 1. The results

show that large amounts of Ru diffused up the temperature gradient and accumulated at the hot ends. Because the temperature at the cold end is much lower, the Ru concentration here is essentially unchanged. Ru is depleted in the middle parts of the samples, leaving a concave-shaped Ru concentration profile. Ru in the low temperature regions could not diffuse sufficiently rapidly to compensate for the loss of Ru in the middle region. After the experiment the Ru concentration should satisfy mass conservation, but it is seen from Fig. 1 that there has been some loss of Ru. This loss might have resulted from severe evaporation at the hot end.

B. Isothermal Annealing Experiment

In order to make sure that the redistribution described above was due to the thermal gradient rather than to reaction of ruthenium with the crucible metal, an isothermal anneal at 2470 K was performed. The Ru concentration in the main part of the sample did not change. Low Ru concentrations on the top and the bottom surfaces are believed to be due to loss by evaporation. From microscopic observation, the original Ru particles on the end surfaces had disappeared leaving holes of the same size. These results show that neither the tungsten crucible nor the rhenium foils influence the distribution of ruthenium in UO_2 during the high temperature experiments. The second phase, which has been identified as URu_3, was observed in the grain boundaries of the UO_2.

4. DISCUSSION

A. Model

Before the experiment, the Ru particles were uniformly distributed in the samples. Under the temperature gradient, the Ru particles dissolve in the UO_2, in which the Ru also diffuses. The redistribution

of ruthenium is governed by the rate of dissolution (or growth) of the metal particles and transport of ruthenium as atomic species in the bulk UO_2. This transport process occurs by ordinary diffusion as well as by thermal diffusion. The model is described in detail in Ref. 7.

B. Comparison of Experiment and Theory

The experimental redistribution profiles and the curves from theory are compared in Fig. 1. The redistribution of Ru in the experiments is relatively more extensive than predicted by the theory. The difference between experiments and theory may have resulted from use of incorrect parameters. For example, the terminal solubility of Ru in UO_2 used in the theoretical computation is an "apparent solubility", which may be much larger than the real solubility of Ru in UO_2[6]. Second, the differences are partly due to the evaporation of Ru on the top of the samples which makes the redistribution of Ru in UO_2 larger.

REFERENCES

1. F. A. Nichols, et al, "Irreversible Thermodynamics in Materials Problems", in Mass Transport Phenomena in Ceramics, Eds. A R. Cooper, et al, Plenum Press, New York (1975).

2. H. Beisswenger, et al, "Thermodiffusion in the System UO_2-CeO_2", J. Nucl. Mater., 21, 38 (1967).

3. L. C. Michels, et al, "In Pile Migration of Fission Product Inclusions in Mixed Oxide Fuels", J. Appl. Phys. 44, 1003 (1973)

4. F. D'annucci, et al, "Migration of Metallic Fission Products in Reactor Oxide Fuels", Nucl. Technol. 35, 80 (1977).

5. J. Bramman, et al, "Redistribution of Fuel and Fission Products in Irradiated Oxide Fuel Pins", J. Br. Nucl. Ener. Soc. 14, 63 (1975).

6. R. L. Yang, "The High Temperature Behavior of Metallic Inclusions in Uranium Oxide", U.S. DOE Report LBL-11117 (1980).

7. S. Y. Zhou and D. R. Olander, LBL-12193 (1981)

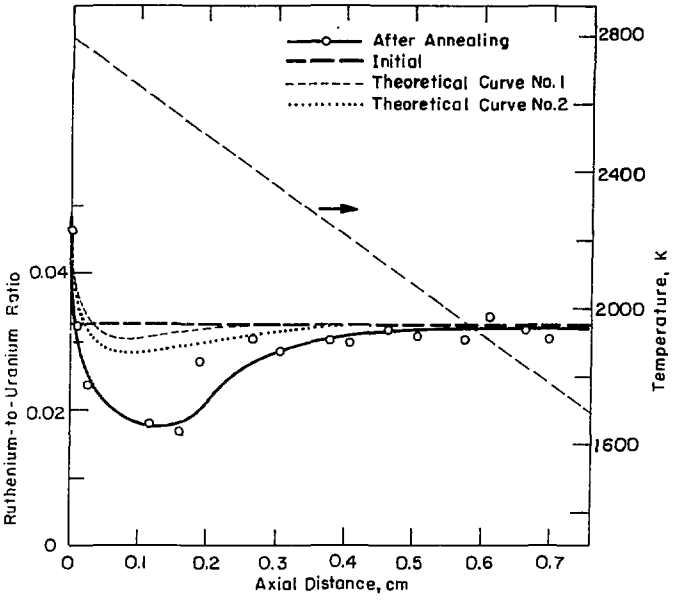

XBL 811-5096

Fig. 1 Redistribution of Ruthenium Along Sample No. 3

T_h = 2780 K; G = 1440 K/cm; L = 0.76 cm, t = 27 hrs

THERMAL-GRADIENT MIGRATION OF BRINE INCLUSIONS IN SALT

A. J. Machiels[+], S. Yagnik

Bedded salt has been proposed as a storage medium for nuclear wastes. Radioactive decay heating of the waste produces temperature gradients in the surrounding salt, which contains ~0.5% water in the form of small cubical brine inclusions. In a thermal gradient, the inclusions migrate towards the heat source. The mechanism of migration is based on the increase of the solubility of salt in water with temperature; in the presence of a temperature gradient across the inclusion, salt dissolves into the inclusion at the hot surface and crystallizes out at the cold surface. Transport by thermal and molecular diffusion of salt within the liquid phase from the hot to the cold faces causes the inclusion to move in the opposite direction. The velocity depends on the temperature coefficient of solubility and interfacial kinetic resistances to dissolution and crystallization.

Experiments have demonstrated that the inclusion speed is controlled principally by the rate of solid dissolution at the hot face of the inclusion. This process, in turn, depends upon the presence of dislocations intersecting the surface which provide the imperfections needed to permit dissolution to occur at small undersaturation of the adjacent liquid. If the hot face of the inclusion were flat on an atomic scale, removal of solid atoms from the perfect surface would be so energetically unfavorable that very large undersaturation would be needed to produce the required dissolution rates. A dislocation which intersects the

[+]Present address University of Illinois, Champaign, IL

*Partially supported by the Office of Nuclear Waste Isolation of the US DOE

dissolving surface provides sites at which the atoms of the solid are less tightly bound than in a perfect atomic plane and hence their removal to the liquid phase is correspondingly easier. A number of experiments support this interpretation:

1. When the mechanical load on the crystal is increased, additional dislocations are created; these interact with the inclusions, causing them to speed up. The effect is not elastic in nature, because the high migration speeds persist when the crystal is unloaded.
2. Experiments were performed in which selected inclusions were subjected to various temperature gradients but the average temperature was not changed. In a liquid diffusion-controlled process or one with linear interface kinetics (e.g. Anthony and Cline's model (1)), the velocity should be proportional to the temperature gradient. However, we found that the velocity varied as the temperature gradient raised to a power > 2. A theoretical model which explains this observation is the Burton, Cabrerra and Frank theory of crystal growth (2) which, when taken in reverse (to model dissolution), predicts a dependence of the velocity on the square of the temperature gradient.
3. If a single inclusion is followed for a long period of time, variations of its velocity by a factor of 4 are observed (Fig. 1). This is attributed to the loss and gain of dislocations at the hot face. In the low dislocation density synthetic crystals used in the experiments, each inclusion face is on the average intersected by less than 3 dislocations. Consequently, loss or gain of one dislocation (for example) can alter the velocity by a substantial

fraction.

The pattern shown on Fig. 1 can be rationalized in the manner shown schematically in Fig. 2. At time zero, the hot face of the inclusion is intersected by a single dislocation (No. 1) close to the center of the face of the inclusion. In general, the dislocation does not intersect the surface at 90° so that as the inclusion moves, the intersection point moves further off-axis. At off-axis positions, the temperature of the surface (and hence the undersaturation of the liquid) is less than it is close to the axis; hence the inclusion slows down. Somewhere between 8 and 20 hours the inclusion picks up another dislocation, designated as No. 2 in Fig. 2. The three dislocation intersections with the dissolving face result in a several-fold increase in the inclusion velocity. As the intersections of the No. 2 dislocation with the hot face move off-axis, the inclusion again begins to slow down.

The dislocation-controlled migration process is qualitatively consistent with all experiments designed to test the hypothesis. It also explains the very large scatter of the measured velocities of small inclusions in crystals of high perfection. Larger inclusions in natural crystals on the other hand are not limited by the number of dislocation intersections at the dissolving face and these inclusions appear to move at the rate predicted by liquid diffusion control.

References:

1. T.R. Anthony and H.E. Cline, J. Appl. Phys. 42, 3380 (1971)

2. P. Bennema and G.H. Gilmer, in "Crystal Growth: an Introduction", P. Hartman, Ed., North-Holland (1973).

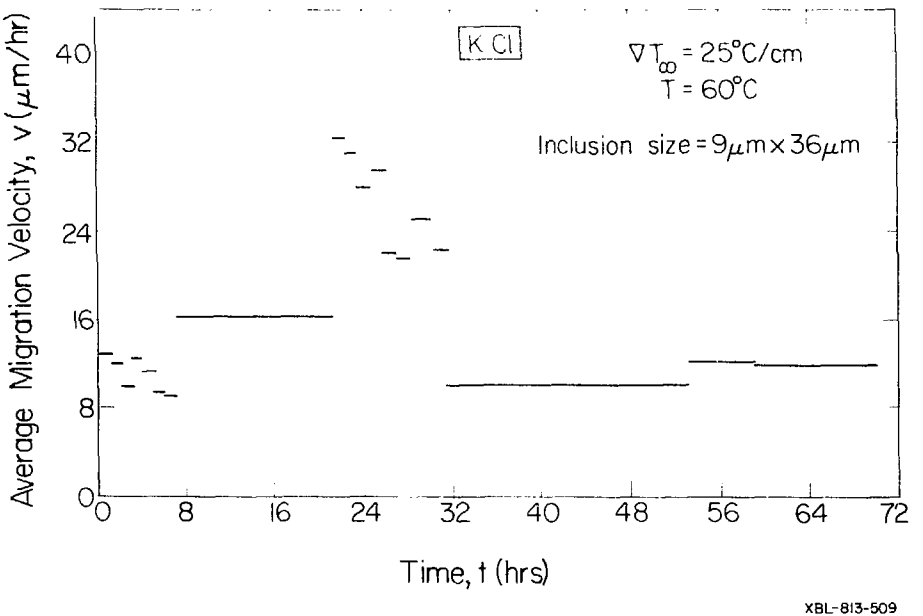

Fig. 1 Variation of the migration velocity of an inclusion in KCl

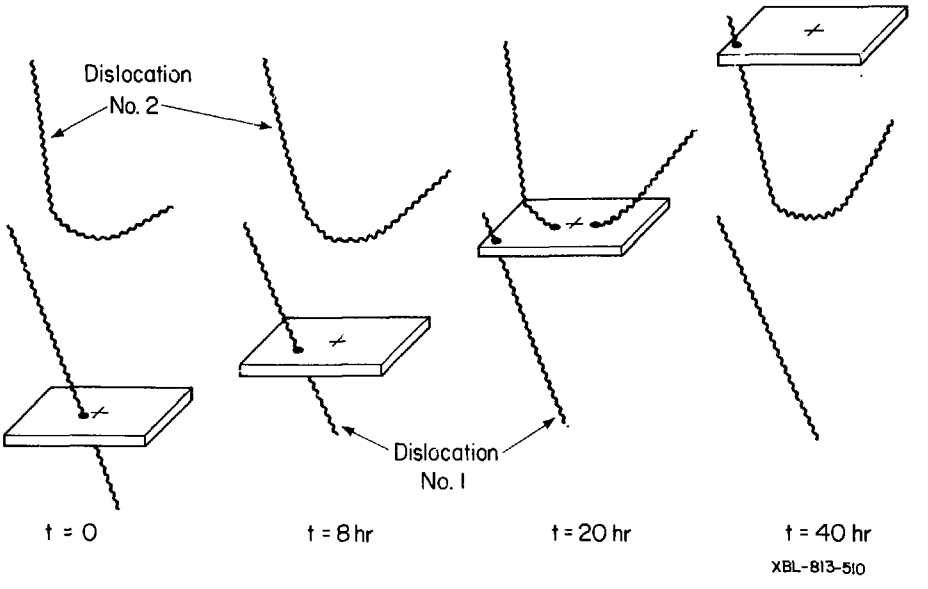

Fig. 2 Schematic explanation of the mechanism of the effect of dislocation intersections on the velocity of inclusions in solids.

TRACER SURFACE DIFFUSION ON UO_2*

D. R. Olander

The coefficient of surface self-diffusion on UO_2 is a key parameter in the processes which affect the behavior of oxide nuclear fuels. Although small fission gas bubbles may not be mobile under normal operating conditions, it is widely believed that in rapid transients gas release is controlled by the motion of these bubbles in the grains. Moreover, their velocity in a temperature gradient is assumed to be governed by the mechanism of surface diffusion, and so the surface diffusivity is an important material property in fuel modeling codes (1-3). This quantity can be measured either by tracer techniques or by mass transfer methods (grain boundary grooving or scratch decay). Maiya's experiments using the latter technique (4) indicated that the grain boundary grooving method is totally evaporation controlled in UO_2 for temperatures above 1700°C.

The only tracer study of surface diffusion on UO_2 is that of Marlowe and Kazanoff (5). This technique for measuring surface diffusivity is shown in Fig. 1. A needle of 93% enriched UO_2 with a flattened point contacted a polished surface of a pellet of depleted UO_2 (0.2% U-235). After a known contact time at a fixed temperature, the radial distribution of tracer was determined by counting the U-234 alpha activity. The experiment was conducted in flowing hydrogen. No transfer of activity from the needle to the pellet was observed when the two were slightly separated. The needle was not sintered to the pellet after the anneal. The tracer spreading data were interpreted in terms of surface diffusion

alone - volume diffusion and gas phase transport were claimed to be unimportant. Robertson (6), using a method proposed by Shewmon (7), corrected the tracer results at 1915°C (the only temperature at which the original data were available) and concluded that the correct value of D_s implied by these data is 300 times larger than the value deduced by Marlowe and Kazanoff, or more than three orders of magnitude larger than the values from the Maiya correlation. Consequently either there is a real physical difference between the mass transfer and tracer methods, or the mathematical interpretation of the tracer spreading data is incorrect. In this study, the latter possibility is examined.

An analysis of surface spreading data which utilizes both the magnitude and the radial variation of the tracer countrate has been developed and implemented numerically. Depletion of the tracer source as well as enrichment of the tracer sink are treated by the model. Parasitic effects such as a contact resistance and evaporation are taken into account. Volume diffusion of tracer is an integral part of the process because it alone permits detection of the tracer transported by surface diffusion. However, volume diffusion does not contribute to radial spreading per se.

Application of the analysis method to the only set of surface spreading data on UO_2 in the literature produces a surface diffusion coefficient (D_s) at 1915°C which is $\sim$ 3000 times larger than that obtained from the same data by the original experimentors and 4 orders of magnitude larger than that obtained by extrapolation of surface diffusivities inferred from mass transfer methods at lower temperatures. The present analysis yields a surface diffusivity between 0.1 and 0.2 cm^2/s at 1915°C. This extreme mobility suggests that UO_2 molecules move on their own surface more like

particles in an ideal gas than by a conventional hopping mechanism. This value of D_s is also very much larger than those used in current fuel modeling codes whose predictions of fission gas release are very sensitive to the value of the surface diffusivity employed.

References:

1. J.R. Matthews and M.H. Wood, J. Nucl. Mater., 84, 125 (1979)
2. J. Rest and S.M. Gehl, 5th Internat. Conf. on Structural Mechanics in Reactor Technology, Berlin, Germany (1979)
3. E.E. Gruber, Nucl. Technol. 35, 617 (1977)
4. P.S. Maiya, J. Nucl. Mater., 40, 57 (1971)
5. M.O. Marlowe and A.I. Kazanoff, J. Nucl. Mater. 25, 328 (1968)
6. W.M. Robertson, J. Nucl. Mater., 30, 36 (1969)
7. P.G. Shewmon, J. Appl. Phys. 34, 755 (1963)

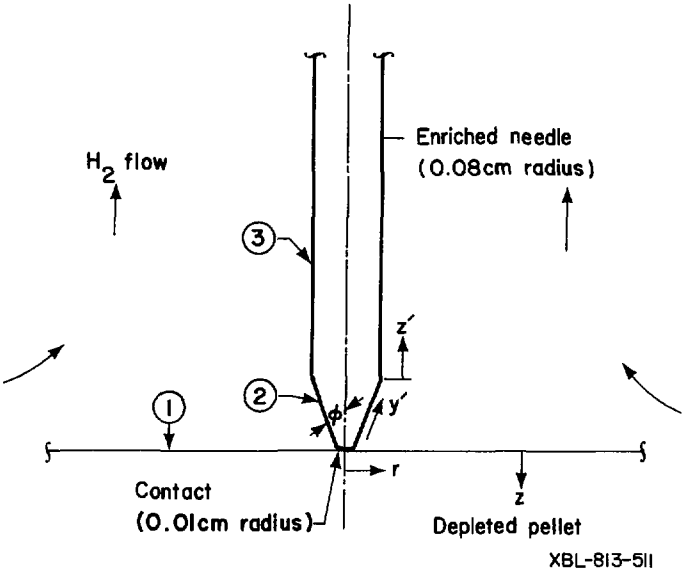

Fig. 1 Tracer method of measuring surface diffusion on UO_2

MOLECULAR BEAM STUDIES OF ATOMIC HYDROGEN REDUCTION OF REFRACTORY OXIDES

by Douglas F. Dooley

During the past year, the modulated molecular beam study of the reduction reactions of thermal atomic hydrogen with the refractory oxides UO_2 and Al_2O_3 were continued and several phases of the experiment were completed. First, data collection on the Al_2O_3 sample was completed. Second, experimentation with the reduced and the stoichiometric UO_2 samples was also concluded. Lastly, investigation of the reduction reaction with hyperstoichiometric urania was initiated.

Data on the reduction of Al_2O_3 were taken at temperatures >1400°C, duplicating prior measurements. Several samples of UO_{2-x} of known stoichiometry (O/U = 1.95 - 2.00) were prepared in a H_2/H_2O furnace. After the samples were sliced and polished, molecular beam data was taken on the hydrogen reduction reaction. Hyperstoichimetric samples were obtained and the experiment is continuing using these samples.

The reaction probability with Al_2O_3 was found to be too low to allow reproducible phase data to be obtained. Reaction probability data for alumina was in general agreement with the previous experimental results. The reduced UO_{2-x} samples were found to be non reactive within the detection limits of the apparatus in the temperature range 200°C - 1800°C. The stoichiometric UO_2 samples were found to be reactive at temperatures $\gtrsim$ 450°C, although near the lower limits of detection. Complete phase, intensity, and temperature scan data were taken on the samples and duplicated until shown to be reproducible. Hyperstoichiometric samples were obtained and experimentation begun with a sample of O/U = 2.036. Reaction probabilities 100 times greater than those of the stoichiometric sample at similar temperatures (e.g. 700°C) were obtained. Data collection is underway.

Experiments with $UO_{2.004}$ are planned after the $UO_{2.036}$ experiment is complete so that the reaction may be studied as a function of O/U ratio. A single crystal UO_2 target is also available to use in an investigation of possible grain boundary effects.